



Two-dimensional Janus drops in shear: deformation, rotation and their coupling

Chun-Yu Zhang¹, Jia-Lei Chen^{1,‡}, Li-Juan Qian² and Hang Ding^{1,†}

¹Department of Modern Mechanics, University of Science and Technology of China, Hefei 230027, PR China

²College of Mechanical and Electrical Engineering, China Jiliang University, Hangzhou 310018, PR China

(Received 11 April 2023; revised 6 November 2023; accepted 13 November 2023)

In this work, the dynamics of two-dimensional rotating Janus drops in shear flow is studied numerically using a ternary-fluid diffuse interface method. The rotation of Janus drops is found to be closely related to their deformation. A new deformation parameter D is proposed to assess the significance of the drop deformation. According to the maximum value of D (D_{max}), the deformation of rotating Janus drops can be classified into linear deformation ($D_{max} \leq 0.2$) and nonlinear deformation ($D_{max} > 0.2$). In particular, D_{max} in the former depends linearly on the Reynolds and capillary numbers, which can be interpreted by a mass–spring model. Furthermore, the rotation period t_R of a Janus drop is found to be more sensitive to the drop deformation than to the aspect ratio of the drop at equilibrium. By introducing a corrected shear rate and an aspect ratio of drop deformation, a rotation model for Janus drops is established based on Jeffery’s theory for rigid particles, and it agrees well with our numerical results.

Key words: suspensions, drops

1. Introduction

Particle-laden flows are seen widely in nature and industrial processes, such as suspensions (Brandt & Coletti 2022), weather forecasting (Li *et al.* 2022) and deep-sea mining (James, Mingotti & Woods 2022). To investigate these complicated multi-phase flows, it is crucial to gain insight into the dynamics at the particle scale so as to interpret the rheological properties and establish dispersed two-phase flow models (Tsai 2022). Here, the particles refer to granules, droplets or bubbles, which have either negligible or finite inertia and a length scale much larger than a micrometre. In particular, suspended particles in a linear

† Email address for correspondence: hding@ustc.edu.cn

‡ Present address: Microsoft Azure AI.

shear flow serves as a flow model for the study of microscopic behaviour of very dilute particulate flows, and has been a longstanding topic of research.

It is known that distinct particles experience very different dynamic processes in shear flows. For example, rigid particles rotate in linear shear flows, and the rotation dynamics is characterised by the shear rate $\dot{\gamma}$ and the aspect ratio λ of the particle (Leal 1980; Voth & Soldati 2017). In particular, an analytical solution of the particle rotation was provided by Jeffery (1922) for ellipsoidal particles, with the assumptions that inertia of both the fluid and particle are negligible, and that the axis of rotation is one of the principal axes of the ellipsoid and also parallel to the vorticity of the shear flow (Cox & Mason 1971). The rotation period t_R and the orientation angle θ of ellipsoidal particles can be correlated to $\dot{\gamma}$ and λ by

$$t_R = 2\pi\dot{\gamma}^{-1}(\lambda + \lambda^{-1}), \quad \theta(t) = \arctan(\lambda^{-1} \tan(\dot{\gamma}t/(\lambda + \lambda^{-1}))). \quad (1.1a,b)$$

Although Jeffery's theory was obtained for ellipsoidal particles (three-dimensional, 3-D), it was found to be independent of the scale of the ellipsoid in the vorticity direction (Zettner & Yoda 2001). Moreover, (1.1a,b) have been shown to give a good prediction of the rotation period for elliptical cylinders (two-dimensional, 2-D) with finite inertia, e.g. in experiments (Zettner & Yoda 2001) and numerical simulations (Aidun, Lu & Ding 1998; Ding & Aidun 2000; Li, Ye & Liu 2016). Later, Jeffery's theory was extended to the rotation prediction of slender particles by introducing an effective shape ratio (Cox 1971). Different leading-order corrections of finite inertia effect to t_R of a neutrally buoyant ellipsoid were also proposed (Mao & Alexeev 2014; Dabade, Marath & Subramanian 2016; Marath & Subramanian 2017). By contrast, droplets/bubbles deform in linear shear flows, and end up resting in steady flows or breaking up when viscous force exerted by the surrounding fluid dominates surface tension (Stone 1994). The dynamics of droplets in shear is characterised by droplet deformation, resulting from the competition among viscous shear, inertia and surface tension (Singh & Sarkar 2011; Singeetham, Chaithanya & Thampi 2021; Yi *et al.* 2022). More specifically, the deformation of a droplet with finite inertia was shown to be linearly dependent on the viscous force arising from the surrounding fluid, for both 2-D (Yue *et al.* 2004; Hu & Adams 2007; Luo, Hu & Adams 2015) and 3-D (Taylor 1932; Liu *et al.* 2021) droplets with small deformations.

More complicated dispersed phases, such as Janus drops, have attracted the attention of researchers, due mainly to their wide applications, e.g. biomedicine (Hao *et al.* 2022), drug delivery (Song *et al.* 2021) and material science (Wei *et al.* 2022). Here, Janus droplets refer to compound drops consisting of two component droplets (of different fluids) in contact. Fluid motion for Janus drops with 'ideal' shape (spherical with a flat, internal interface separating the two droplets of equal size) has been analysed theoretically in the absence of inertia and in the limit of non-deformable interfaces (Shklyaev *et al.* 2013). The Janus drops were found to behave as a simple fluid drop or as a solid body with broken fore and aft symmetry (Díaz-Maldonado & Córdova-Figueroa 2015). Moreover, recent simulations indicated that Janus drops in shear may experience periodical rotation and deformation at the same time, after being formed from the collision between two equal-sized immiscible droplets (Liu & Park 2022). However, flow mechanisms about the dynamics of rotating Janus drops in shear remain unclear, e.g. the coupling between drop deformation and rotation, and the effect of finite inertia on the drop deformation. More importantly, a unified prediction of the rotation period of solid particles and Janus drops has not been explored yet.

Two-dimensional Janus drops in shear

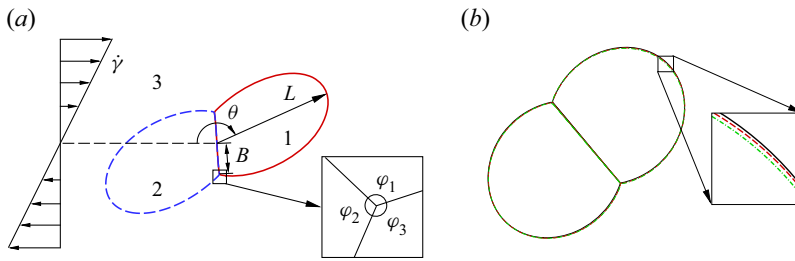


Figure 1. (a) A sketch of a Janus drop in shear flow where φ_i is the interfacial angle of fluid i at the triple-phase line where the ternary fluids meet. (b) Convergence study with respect to the most elongated drop with $Re = 0.2$ and $Ca = 0.05$. Different curves denote the numerical results with different mesh resolutions: $h/R = 0.02$ (dash-dotted), 0.01 (dashed) and 0.005 (solid), respectively. The inset shows a zoomed-in view of the interface.

In this work, the dynamics of 2-D Janus drops in shear flow is studied numerically using a ternary fluid diffuse interface method (Zhang *et al.* 2016). For simplification of the flow problems, we focus on only the Janus drops that have two component droplets with equal size and the same viscosities and surface tensions, as shown in figure 1(a). As a result, the deformation of Janus drops is expected to be rotationally symmetric. A new deformation parameter is proposed to describe the deformation pattern of rotating Janus drops, and different rotation behaviours of Janus drops with small and large deformation are investigated. The correlation among the shear rate, deformation parameter and rotation period of Janus drops is analysed based on the numerical results. Consequently, we establish a theoretical model for rotating Janus drops in a manner similar to that for elliptic rigid particles.

2. Problem statement and numerical methods

2.1. Problem statement

We consider a 2-D neutrally buoyant Janus drop (with density ρ) in shear flow (figure 1a). The Janus drop consists of two immiscible droplets 1 and 2 of equal size πR^2 , where R is the effective radius of the droplets. The Janus drop is located in the middle of two flat plates that move in opposite directions, and is surrounded by fluid 3 in a domain measuring $12R \times 12R$. The initial flow field is $U_0 = ((y - 6)\dot{\gamma}R, 0)$. The two droplets have the same viscosity μ_1 , and fluid 3 has viscosity μ_3 . The surface tension coefficient between fluids i and j is denoted by σ_{ij} . In the present study, we assume $\sigma_{13} = \sigma_{23}$, and vary the value of σ_{12} to get different equilibrium shapes of Janus drops. The geometry parameters of Janus drops are shown in figure 1, including the length of the Janus drop, L , and the length of the internal interface, B . The orientation angle θ is defined as the angle at which the horizontal intersects the line connecting the centres of the two component droplets. Initially, the Janus drop assumes an equilibrium shape, and the corresponding geometry parameters are L_0 and B_0 , which can be obtained analytically from σ_{12}/σ_{13} and the volume $2\pi R^2$, e.g. $L_0 = 1.672R$ and $B_0 = 0.966R$ for $\sigma_{12} = \sigma_{13}$. Details of calculation of L_0 and B_0 can be found in Appendix A. The dynamics can be described by two dimensionless parameters: capillary number $Ca = \mu_3\dot{\gamma}R/\sigma_{13}$, and Reynolds number $Re = \rho\dot{\gamma}R^2/\mu_3$. The ranges of dimensionless parameters investigated in this work are $0.01 \leq Ca \leq 0.8$ and $0.1 \leq Re \leq 2$. Unless stated otherwise, $\mu_1 = \mu_3$ and $\sigma_{12} = \sigma_{13}$ are used in the present study.

2.2. Numerical methods

A ternary fluid diffuse interface method is used to track the interface evolution (Zhang *et al.* 2016). The interfaces are represented by volume fractions of the fluids, $\mathbf{C} = (C_1, C_2)$, where C_i represents the volume fraction of the i th fluid, and $C_1 + C_2 + C_3 = 1$. Time evolution of \mathbf{C} is governed by the dimensionless Cahn–Hilliard equation,

$$\frac{\partial \mathbf{C}}{\partial t} + \nabla \cdot (\mathbf{u}\mathbf{C}) = \frac{1}{Pe} \nabla^2 (\Psi - C_1 C_2 C_3), \quad (2.1)$$

where \mathbf{u} is the flow velocity; the chemical potential $\Psi = (\psi_1, \psi_2)$ is defined as

$$\psi_i = C_i^3 - 1.5C_i^2 + 0.5C_i - Cn^2 \nabla^2 C_i, \quad i = 1, 2, \quad (2.2)$$

where the Cahn number Cn represents a dimensionless measure of the thickness of the diffuse interfaces (Ding, Spelt & Shu 2007). The Cahn number is set to $Cn = 0.7h/R$, so that both a relatively narrow diffuse interface and a well-resolved surface tension can be achieved in simulations, where h is the mesh size. The Péclet number Pe represents the relative significance of convective fluxes to the diffusive fluxes. The diffuse interface model approaches the sharp interface limit with the vanishing of Cn for $Pe \sim Cn^{-1}$ (Magaletti *et al.* 2013), thus $Pe = 1/Cn$ is adopted in the present study. The motion of fluids is governed by the Navier–Stokes equations and the continuity equation. Details about numerical implementation can be found in Zhang *et al.* (2016). The boundary conditions are: no-slip condition at the upper and bottom boundaries with a constant speed $6\dot{\gamma}R$ but in the opposite direction; and periodic condition at the left and right boundaries. The method has been verified quantitatively previously, e.g. compound drop impacting onto a flat plate (Liu *et al.* 2018) and configuration transition of sessile compound drops (Zhang *et al.* 2021). The convergence of numerical results with mesh refinement ($h = 0.02R, 0.01R$ and $0.005R$) is also checked (figure 1*b*), thus $h = 0.01R$ is used in the simulations hereafter.

3. Results and discussion

3.1. Flow regimes of Janus drops in shear flow

Figure 2 shows numerical results of Janus drops and a pure drop in shear flows at $Re = 0.2$, with respect to velocity vectors and interface shapes. Two flow regimes can be identified, namely rotation and breakup, according to the morphology of the Janus drops. In the rotation regime, the drop rotates periodically, accompanied with continuous drop deformation (cf. $Ca = 0.07$ and 0.35 in figures 2*a* and 2*b*, respectively). At relatively small Ca ($= 0.07$), a vortex persists inside the rotating Janus drop, with rotation period $t_R \approx 15.8\dot{\gamma}^{-1}$; at a relatively larger Ca ($= 0.35$), the Janus drop experiences more significant deformation and a longer rotation period ($t_R \approx 42.8\dot{\gamma}^{-1}$). The flow features are also different: only one vortex when the drop is squeezed the most, which also corresponds to the moment of fast rotation; moreover, we can see one vortex contained in each component droplet at the maximum elongation, which implies that the Janus drop rotates very slowly at this moment. As shown in the supplementary movies available at <https://doi.org/10.1017/jfm.2023.963>, the rotation dynamics of the Janus drop at $Ca = 0.35$ is more closely coupled with its deformation than that at $Ca = 0.07$. When Ca is increased further (e.g. $Ca = 0.40$), the Janus drop could elongate continuously and end up with the separation of the two component droplets (see figure 2*c*), i.e. the breakup regime. It is noteworthy that the behaviour of Janus drops in shear is remarkably different from that of pure drops. For

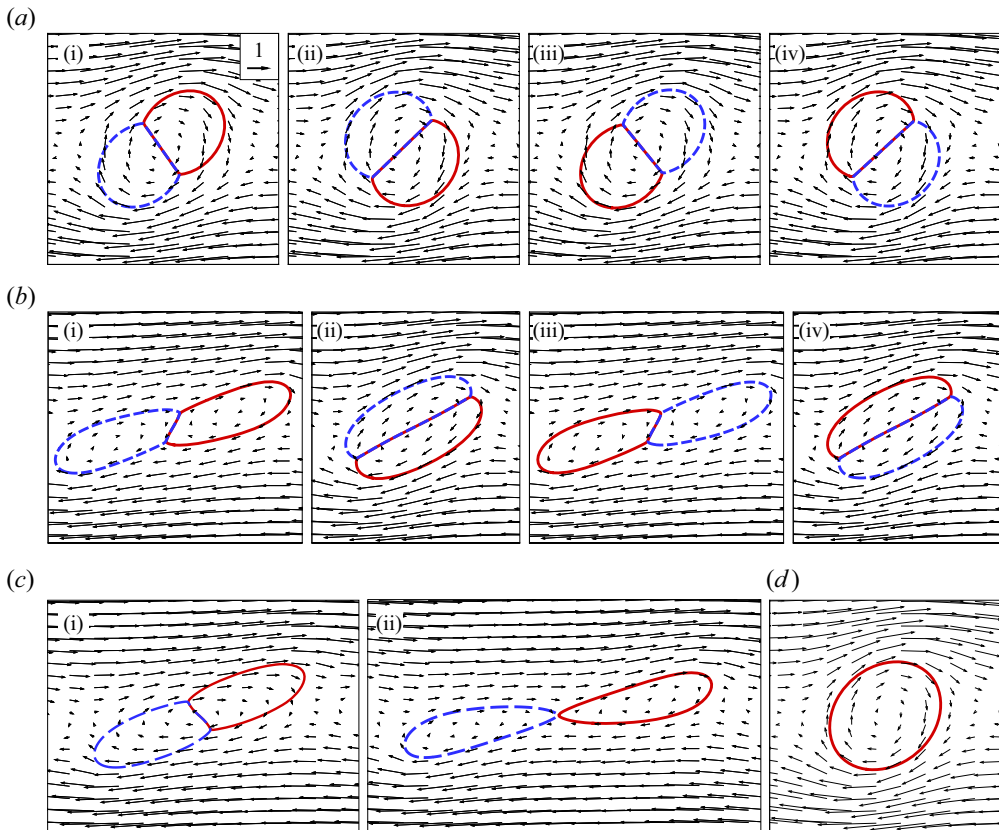


Figure 2. Dynamics of Janus drops and a pure drop in shear flow at $Re = 0.2$. (a) Rotating Janus drop at $Ca = 0.07$. The snapshots from (a*i*–a*iv*) correspond to times $\dot{\gamma}t = 5.4, 10.3, 13.3, 18.2$, respectively. (b) Rotating Janus drop at $Ca = 0.35$. The snapshots are $\dot{\gamma}t = 11.3, 24.7, 32.7, 46.1$ for (b*i*–b*iv*), respectively. (c) Breakup of Janus drops at $Ca = 0.40$. The snapshots correspond to $\dot{\gamma}t = 8.0$ and 30.9 , respectively. (d) Deformed pure drop (of size $2\pi R^2$) in shear flow at $Ca = 0.07$. The reference velocity is shown in (a*i*).

example, a pure drop (of the same size as the Janus drop, $2\pi R^2$) at $Ca = 0.07$ is elongated by shear flow, and moreover, its eventual shape does not change with time (see figure 2*d*).

Figure 3(a) shows the dynamics of a rotating Janus drop at $Re = 0.2$ and $Ca = 0.07$, with respect to the evolution of L and B . We can see that L and B evolve in an anti-phase manner, which means that the maximum value of L (B) and the minimum value of B (L) occur at the same time. The deformation dynamics of the Janus drop is shown in figure 3(b), with respect to the averaged values (\bar{L} and \bar{B}) of the geometry parameters as a function of Ca for different Re . We find $\bar{L} \approx L_0$ and $\bar{B} \approx B_0$ at small Ca (e.g. $Ca < 0.1$), and $\bar{L} > L_0$ and $\bar{B} > B_0$ at relatively large Ca . Herein, we refer to the former as linear deformation, and the latter as nonlinear deformation.

In order to assess quantitatively the deformation and rotation of Janus drops, we define a new deformation parameter,

$$D = \frac{B_0L - L_0B}{B_0L + L_0B}. \quad (3.1)$$

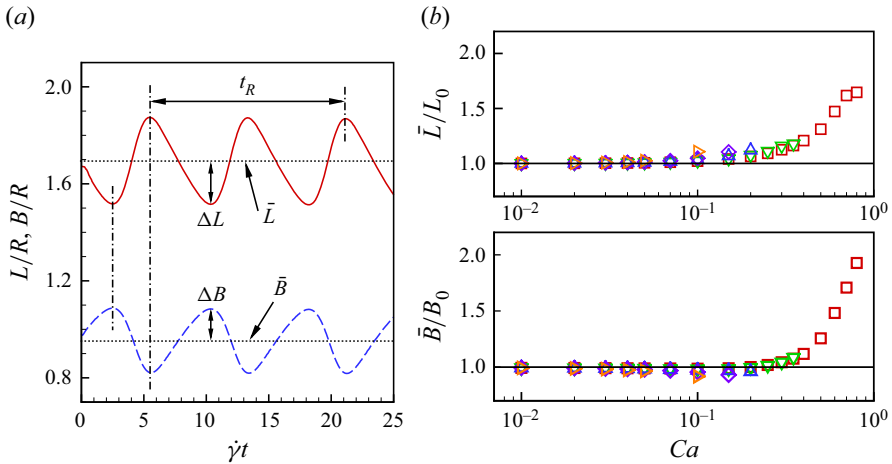


Figure 3. (a) Temporal evolution of L and B at $Re = 0.2$ and $Ca = 0.07$. (b) Numerical results for \bar{L} and \bar{B} for different Re : 0.1 (\square), 0.2 (∇), 0.5 (Δ), 1.0 (\diamond) and 2.0 (\triangleright).

It is straightforward to get $D = 0$ for a Janus drop at equilibrium such that the maximum value of D , D_{max} , occurs at the maximum elongation of the Janus drop and yields

$$D_{max} = \frac{(\bar{L} + \Delta L)B_0 - (\bar{B} - \Delta B)L_0}{(\bar{L} + \Delta L)B_0 + (\bar{B} - \Delta B)L_0}. \tag{3.2}$$

Figure 4 presents the variation of D , the rotation velocity ω ($= d\theta/dt$) and the surface energy E_s of Janus drops in one rotation period with respect to the phase ϕ at $Re = 0.2$ and different Ca , including typical cases of drops with linear deformation ($Ca = 0.07$) and nonlinear deformation ($Ca = 0.35$). Here, $E_s = \int_S \sigma dl$, where S is the area of the drop surface; because $\sigma_{12} = \sigma_{13} = \sigma_{23}$ in this case, E_s is determined solely by the total area of the drop surface. Several observations can be made about figure 4. First, the variation of ω for drops with linear deformation is close to a harmonic function, and has a noticeable phase difference from D . By contrast, the variation of ω for drops with nonlinear deformation deviates significantly from harmonic functions, and appears to synchronize with the change of D . In particular, ω reaches its peak value at the smallest D , and reaches its lowest value (close to zero) at the largest D (namely D_{max}). Second, the occurrence of D_{max} coincides with the apex of E_s . However, the smallest D corresponds not to the lowest E_s , but to the second peak of E_s . Note that the lowest E_s corresponds to $D \approx 0$. From the observations above, we can see that the rotation of Janus drops is coupled with drop deformation, and the coupling is strengthened with increasing Ca . Third, the compression process ($D < 0$) is longer than the elongation one ($D > 0$). This tendency is intensified in the regime of nonlinear deformation.

3.2. Deformation of rotating Janus drops

Deformation of Janus drops reflects the balance between viscous shear, interfacial tension and drop inertia. Figure 5(a) shows that ΔL of all rotating Janus drops can be correlated with Re and Ca by

$$\frac{\Delta L}{R} \propto (1 + \beta Re) Ca, \tag{3.3}$$

Two-dimensional Janus drops in shear

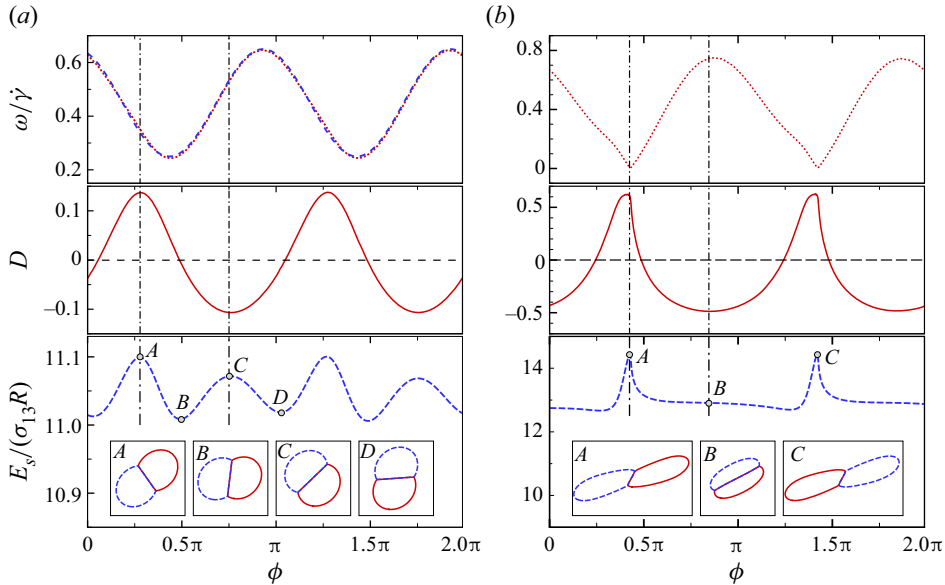


Figure 4. Variation of ω , D and E_S as functions of phase ϕ ($= \theta - \pi/2$) in one rotation period, with $Re = 0.2$ and two different Ca : (a) $Ca = 0.07$ and (b) $Ca = 0.35$. The variation of ω (dotted line) is close to a harmonic function (dashed line). The insets show snapshots of the interfacial shapes of the Janus drops at the extreme points of E_S .

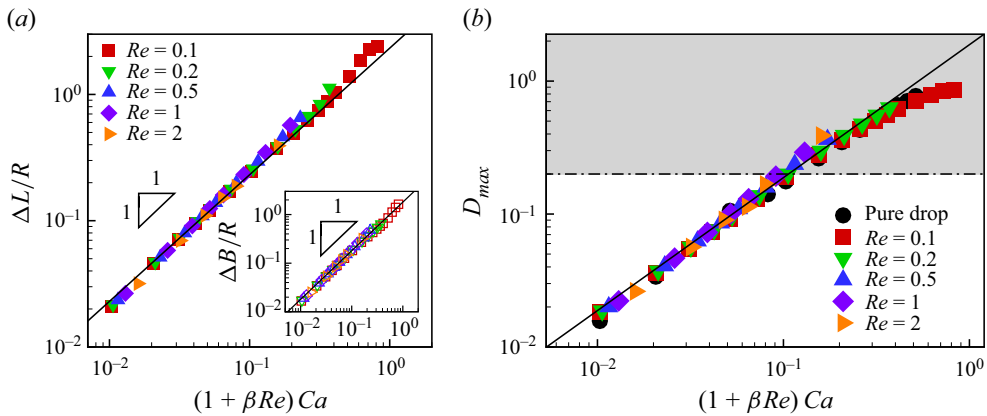


Figure 5. (a) Variation of ΔL as a function of $(1 + \beta Re) Ca$ on a log-log scale. Variation of ΔB is shown in the inset. Different symbols indicate various Reynolds numbers Re : 0.1 (\square), 0.2 (∇), 0.5 (\triangle) and 2.0 (\triangleright). (b) D_{max} as a function of $(1 + \beta Re) Ca$. The solid line represents the (3.5) with $\beta = 0.3$.

where $\beta = 0.3$ is a fitting parameter. Similarly, $\Delta B/R$ is found to have the same proportionality as in (3.3); see the inset of figure 5(a). Moreover, the value of β ($= 0.3$) is also the same for ΔB .

To understand the correlation between ΔL , Re and Ca in (3.3), we model the deformation of Janus drops by a one-dimensional mass–spring system. In this system, the viscosity and inertia of the drop play the roles of the damping elements and the mass, and the surface tension plays the role of the spring. Given the deviation of a Janus drop from its original shape as $L(t) - \bar{L}$, the scales of inertia, viscous damping and surface tension

of the Janus drop can be written as $\rho R^3 \ddot{L}$, $\mu R \dot{L}$ and $\sigma(L - \bar{L})$, respectively. Therefore, the mass–spring system can be expressed as

$$\rho R^3 \ddot{L} + \mu R \dot{L} + \sigma(L - \bar{L}) \sim \mu R^2 \dot{\gamma} + \rho R^4 \dot{\gamma}^2, \quad (3.4)$$

where the two terms on the right-hand side represent the effects of viscous stress and pressure exerted by the surrounding fluid, respectively. Note that \ddot{L} has scale $\Delta L/t_R^2$ and $t_R \gg \dot{\gamma}^{-1}$. Therefore, the effect of drop inertia ($\sim \rho R^3 \Delta L t_R^{-2} \ll \rho R^3 \Delta L \dot{\gamma}^2$) is comparatively negligible. In addition, when the Janus drops are most elongated, we have $\dot{L} = 0$ and $L - \bar{L} = \Delta L$ (by definition). Consequently, at this particular moment, (3.4) can be simplified in dimensionless form as $\Delta L/R \sim Ca + Re Ca$. We note that on the right-hand side of (3.4), the difference in the effective action area between the viscous stress and the pressure is not taken into account. If considering this geometry effect further, then we have $\Delta L/R \propto (1 + \beta Re) Ca$, where β is a geometry factor related to the shape of Janus drops. The value of β is more or less a constant as indicated by the numerical results (see figure 5a).

Figure 5(b) shows the numerical results of D_{max} as a function of $(1 + \beta Re) Ca$ on a log-log scale, including those of pure drops at $Re = 0.1$. The results of stationary pure drops and rotating Janus drops at the maximum elongation collapse onto a single curve. Moreover, D_{max} is proportional to $(1 + \beta Re) Ca$ for $D_{max} \leq 0.2$. This can be explained by simplifying the maximum value of D for Janus drops with linear deformation (denoted by D_{max}^L). Because of $\bar{L} \approx L_0$, $\bar{B} \approx B_0$ and $|B_0 \Delta L - L_0 \Delta B| \ll 2L_0 B_0$ (which can be derived from $D_{max} \ll 1$), we can obtain $D_{max}^L \approx (\Delta L/L_0 + \Delta B/B_0)/2$. Given the correlation of ΔL and ΔB with Re and Ca , we can obtain directly

$$D_{max}^L \propto (1 + \beta Re) Ca. \quad (3.5)$$

Rotating Janus drops can thus be classified quantitatively according to the value of D_{max} , i.e. $D_{max} \leq 0.2$ for linear deformation, and $D_{max} > 0.2$ for nonlinear deformation. More precisely, the linear dependence of D_{max} on Re and Ca holds for $(1 + 0.3 Re) Ca \leq 0.1$ in the present study. We note that the linear relation in (3.5) is also found to be valid for Janus drops with different initial shapes (by changing σ_{12}/σ_{13}), in the case of small deformations.

3.3. Coupling between rotation period and drop deformation

Figure 6(a) shows the variation of t_R for Janus drops at $Re = 0.2$ with different equilibrium shape (measured by L_0/B_0). For Janus drops with linear deformation (e.g. $Ca = 0.02$), t_R increases only slowly with L_0/B_0 , which is very different from the effect of aspect ratio of particles on t_R , as given in (1.1a,b). By contrast, a quick increase of t_R with L_0/B_0 is observed for those with nonlinear deformation (e.g. $Ca = 0.1$ and $L_0/B_0 > 2$). Therefore, for Janus drops, the change of aspect ratio due to drop deformation determines the rotation period, rather than the equilibrium shape of the drop. Figures 6(b) and 6(c) show the variation of t_R and D_{max} for Janus drops with different viscosity. At low Ca (< 0.1), t_R and D_{max} maintain more or less the same value, although the viscosity of Janus drops undergoes a change of two orders in magnitude. At relatively high Ca (> 0.1), the Janus drop with higher viscosity (e.g. $\mu_1/\mu_3 = 10$) can resist the shear flow with less deformation, leading to an insignificant increase of D_{max} (and t_R) with Ca . Figure 7(a) shows the variation of t_R with Ca at different Re . At the same Re , t_R maintains an approximately constant value at low Ca , and increases rapidly with Ca at relatively large Ca (i.e. for drops with nonlinear deformation).

Two-dimensional Janus drops in shear

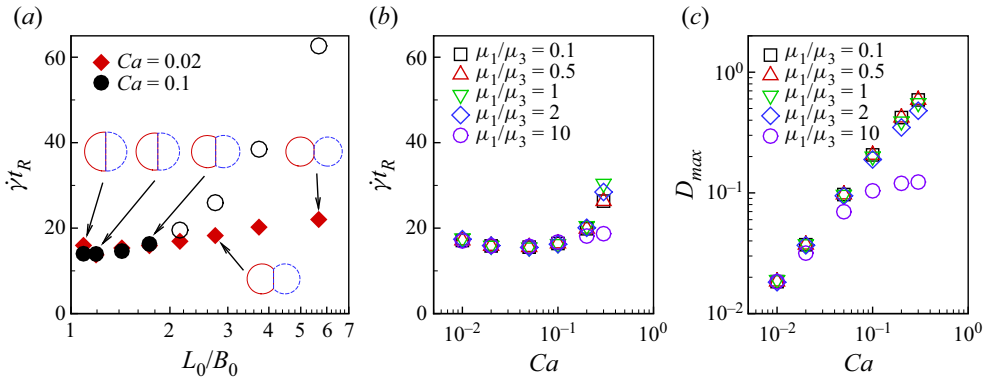


Figure 6. (a) Variation of t_R for Janus drops with different L_0/B_0 at $Re = 0.2$ and $\mu_1/\mu_3 = 1$. The empty symbols represent the nonlinear deformation, and the filled symbols represent the linear deformation. Variation of (b) t_R and (c) D_{max} at $Re = 0.2$ for $L_0/B_0 (= 1.732)$ and various μ_1/μ_3 : 0.1 (\square), 0.5 (\triangle), 1 (∇), 2 (\diamond) and 10 (\circ).

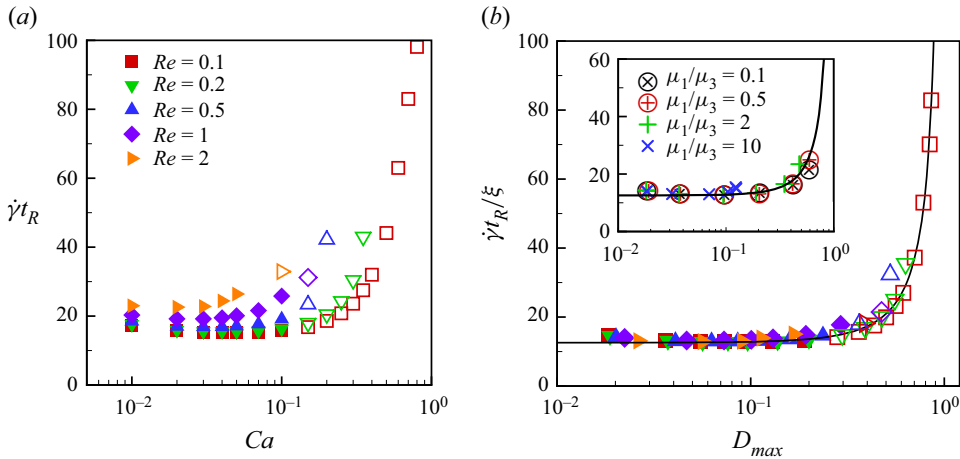


Figure 7. (a) Rotating period as a function of Ca , with $\mu_1 = \mu_3$ and various Re . (b) The comparison of t_R between numerical results in (a) and theoretical prediction of (3.8) (denoted by the solid line). The inset shows the results for different μ_1/μ_3 with $Re = 0.2$. In (a,b), the filled and empty symbols denote the cases $D_{max} \leq 0.2$ and $D_{max} > 0.2$, respectively.

The rotation of Janus drops is similar to that of particles, except for flow slip at the interfaces and deformable shape. The slip effect at the drop interface can be approximated by a corrected shear rate $\dot{\gamma}/\xi$, where the correction is $\xi \geq 1$. Based on theoretical analysis of t_R of a fluid sphere and a spherical particle in shear flow at $Re = 0$, Bartok & Mason (1958) obtained $\xi = 2/\sqrt{3}$ for the fluid sphere with matched viscosity, which is adopted in the present study. To take the effect of finite inertia further into account, ξ can be approximated to the first order of Re by

$$\xi \approx \frac{2}{\sqrt{3}} + \frac{d\xi}{dRe} Re. \quad (3.6)$$

The deformations of rotating Janus drops are characterised by the maximum elongation. An effective aspect ratio of Janus drops, λ_J , is thus defined by the geometry parameters of

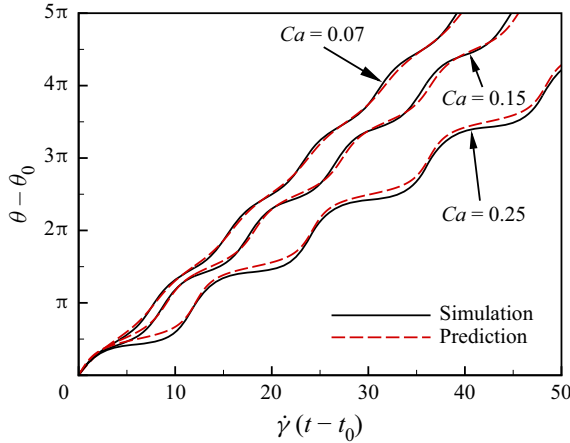


Figure 8. Comparison between the results of simulation and (3.9) of $\theta - \theta_0$ as a function of $\dot{\gamma}(t - t_0)$ at $Re = 0.2$ and various Ca .

Janus drops at that moment:

$$\lambda_J = \frac{(\bar{B} - \Delta B)L_0}{(\bar{L} + \Delta L)B_0} = \frac{1 - D_{max}}{1 + D_{max}}. \tag{3.7}$$

In this aspect ratio model, it is straightforward to have $\lambda_J = 1$ for Janus drops at equilibrium (i.e. $D_{max} = 0$) regardless of their differences in shape, which reflects the dominant effect of drop deformation on the rotation period.

Jeffery’s theory (1.1a,b) was shown to be applicable to elliptical cylinders (Ding & Aidun 2000; Zettner & Yoda 2001). Following the spirit of Jeffery’s theory, the rotation period of 2-D Janus drops can be obtained by introducing a corrected $\dot{\gamma}$ and an effective aspect ratio λ_J . That is,

$$t_R \dot{\gamma} = 2\pi\xi(\lambda_J + \lambda_J^{-1}) = 4\pi\xi \frac{1 + D_{max}^2}{1 - D_{max}^2}. \tag{3.8}$$

Figure 7(b) shows the variation of $t_R \dot{\gamma} / \xi$ as a function of D_{max} . Numerical results for Janus drops agree well with the theoretical prediction with a fitting of $d\xi/dRe = 0.3$. Because (3.8) is consistent with the calculation of t_R in (1.1a,b), the rotation period of particles and Janus drops can be predicted in a unified manner.

Similarly, we can obtain the theoretical prediction of θ :

$$\theta - \theta_0 = \arctan \left(\frac{1 + D_{max}}{1 - D_{max}} \tan \left(\frac{\dot{\gamma}(t - t_0)}{2\xi} \frac{1 - D_{max}^2}{1 + D_{max}^2} \right) \right), \tag{3.9}$$

where an initial value θ_0 ($= \pi/2$) and the corresponding time t_0 are introduced to avoid the start-up effect in numerical simulations. Figure 8 shows the time variation of θ of rotating Janus drops at $Re = 0.2$ and different Ca . The numerical results agree well with the theoretical prediction for drops with linear deformation ($Ca = 0.07$), but deviate from it slightly for drops with nonlinear deformation ($Ca = 0.15$ and 0.25), owing to the synchronization of rotation velocity ω with drop deformation.

4. Conclusion

We simulate the dynamics of a 2-D Janus drop in shear flows, with a focus on the deformation, rotation and their coupling. A new deformation parameter is proposed to describe the deformation of the Janus drop. Two flow regimes, i.e. linear deformation and nonlinear deformation, are identified according to the maximum value of D , D_{max} . In the regime of linear deformation ($D_{max} \leq 0.2$), the time variation of the rotation velocity ω of the Janus drop is a harmonic function, and has a noticeable phase difference from that of D ; moreover, D_{max} is proportional to $(1 + \beta Re) Ca$, which can be interpreted by a mass–spring model. In the regime of nonlinear deformation ($D_{max} > 0.2$), the rotation velocity of the Janus drop is synchronized with D , showing a close coupling between the deformation and rotation. In addition, we find that the rotation period t_R of a Janus drop is more sensitive to the deformation than to the aspect ratio of drop at equilibrium, and that the effect of the viscosity of the Janus drop on t_R is also related to the drop deformation. In order to compare with the rotation of elliptic particles, we take the effect of a slip condition at the interface and drop deformation into account, by introducing a corrected shear rate $\dot{\gamma}/\xi$ and an aspect ratio of drop deformation λ_J . Then a rotation model for Janus drops is established based on the Jeffery’s theory for rigid particles. This rotation model gives an excellent prediction of our numerical results within the parameter ranges $0.1 \leq Re \leq 2$ and $0.01 \leq Ca \leq 0.8$, which includes the range of linear and nonlinear deformations, and is before the onset of breakup of Janus drops.

In the present study, we consider the dynamics of only 2-D Janus drops in shear flow. For 3-D Janus drops, it is reasonable to expect that they would display similar dynamic behaviours to 2-D ones, such as rotation and breakup, if the inner interface is parallel to the vorticity of the shear flow; otherwise, one may wonder if they move on a trajectory similar to Jeffery’s orbits observed for ellipsoidal particles, probably accompanied with drop deformation. This will be our future research topic.

Supplementary movies. Supplementary movies are available at <https://doi.org/10.1017/jfm.2023.963>.

Funding. We are grateful for the support of the National Natural Science Foundation of China (grant nos 11932019, 12293002, 12388101).

Declaration of interests. The authors report no conflict of interest.

Author ORCIDs.

 Chun-Yu Zhang <https://orcid.org/0000-0002-2685-7622>;

 Hang Ding <https://orcid.org/0000-0002-7395-6332>.

Appendix A. Calculation of L_0 and B_0 for Janus drops at equilibrium

The shape of Janus drops at equilibrium is determined by the drop size and the surface tensions. [Figure 9](#) shows a sketch of the interface shape of a 2-D Janus drop at equilibrium. Considering the balance of surface tensions at the triple-phase line where the ternary fluids meet, we have (Zhang *et al.* 2016)

$$\frac{\sin \varphi_1}{\sigma_{23}} = \frac{\sin \varphi_2}{\sigma_{13}} = \frac{\sin \varphi_3}{\sigma_{12}}, \quad (\text{A1})$$

where φ_i represents the interfacial angle of fluid i (as shown in [figure 1a](#)), and clearly, $\varphi_1 + \varphi_2 + \varphi_3 = 2\pi$. In the present study, we consider only $\sigma_{13} = \sigma_{23}$, thereby leading to $\varphi_1 = \varphi_2 = \arccos(-\sigma_{12}/(2\sigma_{13}))$ and $\varphi_3 = 2\pi - 2\varphi_1$.

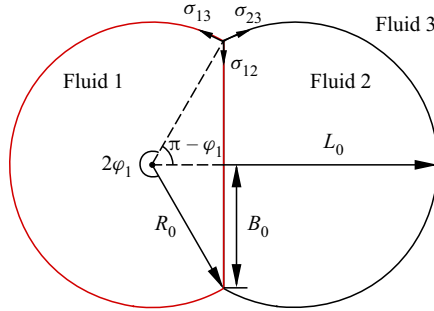


Figure 9. Sketch of a 2-D Janus drop at equilibrium.

At equilibrium, the shape of the component droplets assumes a circular segment. Because the two droplets have equal size, the area of the circular segment yields $(\varphi_1 - \sin \varphi_1 \cos \varphi_1)R_0^2 = \pi R^2$, where R_0 is the radius of the circular segment. Therefore, R_0 can be expressed as

$$R_0 = R \sqrt{\frac{\pi}{\varphi_1 - \sin \varphi_1 \cos \varphi_1}}. \quad (\text{A2})$$

Geometrically, we have $L_0 = R_0(1 - \cos \varphi_1)$ and $B_0 = R_0 \sin \varphi_1$. Thus L_0 and B_0 can be calculated by

$$L_0 = R(1 - \cos \varphi_1) \sqrt{\frac{\pi}{\varphi_1 - \sin \varphi_1 \cos \varphi_1}}, \quad B_0 = R \sin \varphi_1 \sqrt{\frac{\pi}{\varphi_1 - \sin \varphi_1 \cos \varphi_1}}. \quad (\text{A3a,b})$$

REFERENCES

- AIDUN, C.K., LU, Y.N. & DING, E.J. 1998 Direct analysis of particulate suspensions with inertia using the discrete Boltzmann equation. *J. Fluid Mech.* **373**, 287–311.
- BARTOK, W. & MASON, S.G. 1958 Particle motions in sheared suspensions: VII. Internal circulation in fluid droplets (theoretical). *J. Colloid Sci.* **13**, 293–307.
- BRANDT, L. & COLETTI, F. 2022 Particle-laden turbulence: progress and perspectives. *Annu. Rev. Fluid Mech.* **54**, 159–189.
- COX, R.G. 1971 The motion of long slender bodies in a viscous fluid. Part 2. Shear flow. *J. Fluid Mech.* **45**, 625–657.
- COX, R.G. & MASON, S.G. 1971 Suspended particles in fluid flow through tubes. *Annu. Rev. Fluid Mech.* **3**, 291–316.
- DABADE, V., MARATH, N.K. & SUBRAMANIAN, G. 2016 The effect of inertia on the orientation dynamics of anisotropic particles in simple shear flow. *J. Fluid Mech.* **791**, 631–703.
- DÍAZ-MALDONADO, M. & CÓRDOVA-FIGUEROA, M. 2015 On the anisotropic response of a Janus drop in a shearing viscous fluid. *J. Fluid Mech.* **770**, R2.
- DING, E.J. & AIDUN, C.K. 2000 The dynamics and scaling law for particles suspended in shear flow with inertia. *J. Fluid Mech.* **423**, 317–344.
- DING, H., SPELT, P.D.M. & SHU, C. 2007 Diffuse interface model for incompressible two-phase flows with large density ratios. *J. Comput. Phys.* **226**, 2078–2095.
- HAO, X., DU, T., HE, H., YANG, F., WANG, Y., LIU, G. & WANG, Y. 2022 Microfluidic particle reactors: from interface characteristics to cells and drugs related biomedical applications. *Adv. Mater. Interfaces* **9**, 2102184.
- HU, X.Y. & ADAMS, N.A. 2007 An incompressible multi-phase SPH method. *J. Comput. Phys.* **227**, 264–278.
- JAMES, C.B.G., MINGOTTI, N. & WOODS, A.W. 2022 On particle separation from turbulent particle plumes in a cross-flow. *J. Fluid Mech.* **932**, A45.
- JEFFERY, G. 1922 The motion of ellipsoidal particles immersed in a viscous fluid. *Proc. R. Soc. Lond. A* **102**, 161–179.

- LEAL, L.G. 1980 Particle motions in a viscous-fluid. *Annu. Rev. Fluid Mech.* **12**, 435–476.
- LI, C., LIM, K., BERK, T., ABRAHAM, A., HEISEL, M., GUALA, M., COLETTI, F. & HONG, J. 2022 Settling and clustering of snow particles in atmospheric turbulence. *J. Fluid Mech.* **912**, A49.
- LI, C.G., YE, M. & LIU, Z.M. 2016 On the rotation of a circular porous particle in 2D simple shear flow with fluid inertia. *J. Fluid Mech.* **808**, R3.
- LIU, H.-R., NG, C.S., CHONG, K.L., LOHSE, D. & VERZICCO, R. 2021 An efficient phase-field method for turbulent multiphase flows. *J. Comput. Phys.* **446**, 110659.
- LIU, H.-R., ZHANG, C.-Y., GAO, P., LU, X.-Y. & DING, H. 2018 On the maximal spreading of impacting compound drops. *J. Fluid Mech.* **854**, R6.
- LIU, W.K. & PARK, J.M. 2022 Ternary modeling of the interaction between immiscible droplets in a confined shear flow. *Phys. Rev. Fluids* **7**, 013604.
- LUO, J., HU, X.Y. & ADAMS, A. 2015 A conservative sharp interface method for incompressible multiphase flows. *J. Comput. Phys.* **284**, 547–565.
- MAGALETTI, F., PICANO, F., CHINAPPI, M., MARINO, L. & CASCIOLA, C.M. 2013 The sharp-interface limit of the Cahn–Hilliard/Navier–Stokes model for binary fluids. *J. Fluid Mech.* **714**, 95–126.
- MAO, W. & ALEXEEV, A. 2014 Motion of spheroid particles in shear flow with inertia. *J. Fluid Mech.* **749**, 145–166.
- MARATH, N.K. & SUBRAMANIAN, G. 2017 The effect of inertia on the time period of rotation of an anisotropic particle in simple shear flow. *J. Fluid Mech.* **830**, 165–210.
- SHKLYAEV, S., IVANTSOV, A.O., DÍAZ-MALDONADO, M. & CÓRDOVA-FIGUEROA, U.M. 2013 Dynamics of a Janus drop in an external flow. *Phys. Fluids* **25**, 082105.
- SINGEETHAM, P.K., CHAITHANYA, K.V.S. & THAMPI, S.P. 2021 Dilute dispersion of compound particles: deformation dynamics and rheology. *J. Fluid Mech.* **917**, A2.
- SINGH, R.K. & SARKAR, K. 2011 Inertial effects on the dynamics, streamline topology and interfacial stresses due to a drop in shear. *J. Fluid Mech.* **683**, 149–171.
- SONG, Q., CHAO, Y., ZHANG, Y. & SHUM, H.C. 2021 Controlled formation of all-aqueous Janus droplets by liquid–liquid phase separation of an aqueous three-phase system. *J. Phys. Chem. B* **125**, 562–570.
- STONE, H.A. 1994 Dynamics of drop deformation and breakup in viscous fluids. *Annu. Rev. Fluid Mech.* **26**, 65–102.
- TAYLOR, G.I. 1932 The viscosity of a fluid containing small drops of another fluid. *Proc. R. Soc. A* **138**, 41–48.
- TSAI, S.T. 2022 Sedimentation motion of sand particles in moving water (i): the resistance on a small sphere moving in non-uniform flow. *Theor. Appl. Mech. Lett.* **12** (6), 100392.
- VOTH, G.A. & SOLDATI, A. 2017 Anisotropic particles in turbulence. *Annu. Rev. Fluid Mech.* **49**, 249–276.
- WEI, W.S., JEONG, J., COLLINGS, P.J. & TODH, A.G. 2022 Focal conic flowers, dislocation rings, and undulation textures in smectic liquid crystal Janus droplets. *Soft Matt.* **18**, 4360–4371.
- YI, L., WANG, C., VAN VUREN, T., LOHSE, D., RISSO, F., TOSCHI, F. & SUN, C. 2022 Physical mechanisms for droplet size and effective viscosity asymmetries in turbulent emulsions. *J. Fluid Mech.* **951**, A39.
- YUE, P.T., FENG, J.J., LIU, C. & SHEN, J. 2004 A diffuse-interface method for simulating two-phase flows of complex fluids. *J. Fluid Mech.* **515**, 293–317.
- ZETTNER, C.M. & YODA, M. 2001 Moderate-aspect-ratio elliptical cylinders in simple shear with inertia. *J. Fluid Mech.* **442**, 241–266.
- ZHANG, C.Y., DING, H., GAO, P. & WU, Y.L. 2016 Diffuse interface simulation of ternary fluids in contact with solid. *J. Comput. Phys.* **309**, 37–51.
- ZHANG, C.-Y., GAO, P., LI, E.-Q. & DING, H. 2021 On the compound sessile drops: configuration boundaries and transitions. *J. Fluid Mech.* **917**, A37.